Failure Mechanisms of Plasterboard in Nail Pull Test Determined by X-ray Microtomography and Digital Volume Correlation

Amine Bouterf, Jérôme Adrien, Eric Maire, Xavier Brajer, François Hild, Stéphane Roux

To cite this version:

Amine Bouterf, Jérôme Adrien, Eric Maire, Xavier Brajer, François Hild, et al.. Failure Mechanisms of Plasterboard in Nail Pull Test Determined by X-ray Microtomography and Digital Volume Correlation. Experimental Mechanics, 2016, 56, pp.1427 - 1437. 10.1007/s11340-016-0168-8 . hal-01383905

HAL Id: hal-01383905

https://hal.science/hal-01383905v1

Submitted on 19 Oct 2016

Failure mechanisms of plasterboard in nail pull test determined by X-ray microtomography and digital volume correlation

A. Bouterf*, [a,c], J. Adrien [b] E. Maire [b] X. Brajer [c] F. Hild [a]
S. Roux [a]

[a]*LMT-Cachan, ENS Cachan/CNRS/Université Paris-Saclay*
61 avenue du Président Wilson, 94235 Cachan Cedex, France
**Corresponding author. Email: amine.bouterf@lmt.ens-cachan.fr*

[b]*MATEIS-INSA de Lyon, Bât. B. Pascal*
7 avenue Jean Capelle, 69621 Villeurbanne Cedex, France

[c]*Saint-Gobain Recherche, 39 quai Lucien Lefranc*
BP 135, 93303 Aubervilliers Cedex, France

Abstract

To design lightweight plasterboard and optimize the compromise between thermal resistance and mechanical strength, it is important to characterize its strength as characterized with the normative "Nail pull" test. Understanding the phenomenology of this test is the key to identifying the limiting factor in terms of load carrying capacity. In this work, the degradation mechanisms of lightweight plasterboard are analyzed via tests conducted in-situ in a laboratory tomograph. Through the analysis of the kinematics by digital volume correlation, the different mechanisms at play up to failure mechanism have been identified, i.e., quasi-elastic regime, failure of the roller coating layer, core compaction and core failure. The compaction of the core by the collapse of porosity in compression is recognized as the limiting factor in terms of compressive strength and tearing resistance.

Keywords: Digital volume correlation, lightweight plasterboard, nail pull test, X-ray tomography

1 Introduction

Gypsum boards are sandwiches composed of a core of plaster cast between two paper layers. They are finishing products very commonly used in construction. Gypsum is a material particularly suited to indoor use due to its thermal and acoustic insulation properties in addition to its fire resistance. The social demand for reducing the carbon footprint and energy consumption of plasterboard manufacturing is a strong motivation for innovation. Lightening the material through the incorporation of foam in the stucco slurry is thus a natural trend. It requires a good control of the chemical formulation and additives, the setting conditions and the overall industrial processes so as to preserve the performance level on all required properties.

In addition to its fire resistance, lightweight plasterboard must meet mechanical requirements [1]. The *flexural strength* is essential for the transport, handling and installation of the board. *Hardness* characterizes the ability to preserve the surface geometric integrity after shocks and contacts. The third and last property that is considered is the *nail pull strength* or *tear resistance.* This quantity defines the ability of the board to be nailed or screwed. This third property is the most severe to meet for light plasterboards. The nail pull resistance remains the essential condition that prevents a significant decrease in surface density of plasterboard beyond the current level ranging from 7.2 to

8.2 kg/m^2 for 12.7 mm-thick plates [2,3]. This constitutes a strong motivation for understanding the physical phenomena at play in the damage and failure mechanism of the nail pull test. The final aim for industry is to optimize the stucco microstructure, the foam characteristics or the fabrication process to address the relevant features to enhance the mechanical properties.

The American standard ASTM C473 [1] describes the conventional methods for physical testing of gypsum boards. The nail pull test aims at quantifying the perforation resistance of gypsum board with a nail head. The diameter of the nail is equal to 2.515 ± 0.076 mm and that of the head is 6.35 ± 0.127 mm. Two methods of perforation are described. The first is carried out by hand, with a lever arm, considered to be with constant force. The second is conducted on a tension/compression testing machine with constant speed of the nail (i.e. 25 mm/min). The value given for the nail pull resistance is the maximum load when the head of the nail penetrates through plasterboard. According to the ASTM C1396 standard [4], a minimum load level of 350 N has to be reached for 12.7-mm thick plates.

The mechanical behavior of plasterboard in nail pull tests is still debated [5,3,6–8]. If some phenomena are usually reported (e.g. top paper surface perforation, plaster foam crushing, cone and radial cracking) their sequential or simultaneous character and how they relate to the load/penetration curve are difficult to assess. In most of the reported studies, the mechanism of failure is deduced from the analysis of the macroscopic response curve and also from post-mortem or interrupted test analyses of the specimen that are delicate. The interplay of the different phenomena remains to be elucidated precisely.

X-ray computed tomography (X-CT) is valuable for the 3D inspection of material microstructures (especially for porous media) in a non-destructive and non-intrusive way [15–17,9]. It therefore constitutes a unique opportunity to have an exhaustive characterization of the different stages of damage and failure controlling the nail pull strength. However, a number of acquisitions are required through a test and, ideally, such tests are performed in-situ. This is precisely the objective of the present study.

One key improvement provided by computed tomography is that the *same* sample can be imaged in the bulk at different levels of load. For some materials (e.g. sand), the fact that the sample is unloaded to be imaged *ex-situ* does not significantly change the sought information (i.e. density maps [18]) provided the hydrostatic confinement is still applied. Tomodensitometric measurements allowed Desrues et al. [19] to study the complex pattern of localization bands in the bulk of sand samples. The development of *in-situ* mechanical experiments coupled with X-ray tomography began with the observations of crack openings in aluminum alloy [20]. Mechanical tests coupled with *in-situ* tomographic observations have subsequently been developed [21–23]. Significant progress has been made in the design of new testing setups and more importantly on the understanding of various degradation mechanisms that could only be revealed thanks to observations in the bulk of materials.

Reconstructed X-ray tomography volumes can be quantitatively analyzed via Digital Volume Correlation (DVC) [21,24,26–30] to measure the displacement fields in the bulk of samples. DVC is the 3D extension of digital image correlation [25] whereby displacement fields are measured by registering sub-volumes in the deformed configuration with those in the reference configuration. Being based on 3D gray level valued images, DVC provides three dimensional displacement fields. Global approaches in which the displacement field is interpolated via finite element discretizations have been introduced later on [31].

In the following study, a regularized approach will be utilized [35,36].

After a detailed description of the experimental procedure used herein, the failure mechanisms of lightweight plasterboard are discussed by comparing the load-displacement curve recorded during the test and the in-situ tomographic observations. In addition, Digital Volume Correlation (DVC) is used to measure the three dimensional displacement field all along the test.

2 Experimental study

2.1 Studied material

The studied material is lightweight plasterboard mainly composed of a foamed plaster core surfaced with two paper linings. The main function of the two paper layers is to carry the tensile stresses and to protect the sandwich core. The foamed core mainly contributes to the rigidity of the board and to bear shear loadings. It also provides the compressive strength. At the interface between the paper facing and the core plaster foam, a thin layer of dense gypsum (i.e. unfoamed plaster) referred to as "roller coating" is introduced at the fabrication stage to provide an enhanced hardness as well as tensile/flexural strength. Adhesion between the paper and the gypsum core is promoted by the addition of starch. The latter has definite advantages over other binders, such as epoxy and phenolic components, in construction applications, as it is readily available, environmentally friendly, inexpensive and renewable.

Figure 1 shows a slice through a tomographic image volume that reveals the different components of lightweight plasterboard.

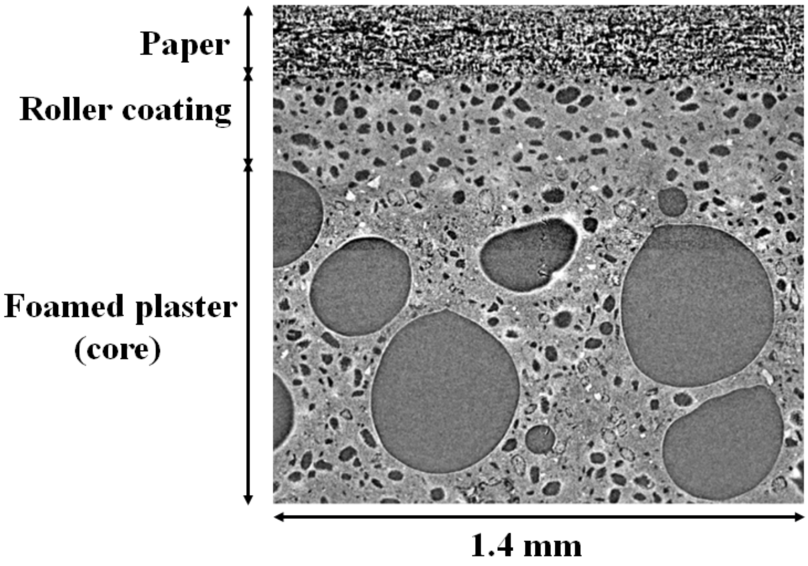

Fig. 1. Main components of lightweight plasterboard revealed thanks to a microtomographic section

This scan was acquired at beamline ID19 of the European Synchrotron Radiation Facility (ESRF, Grenoble, France) at a resolution of 1.4 µm. The studied plasterboard has a very high pore volume fraction (about 75%). The higher density of the roller coating layer is easily recognized. The microstructure of the foam is complex and multi-scale. Well-formed, round pores issued from the foam incorporation are observed with diameters ranging from 200 to 500 µm. Their surface consists of gypsum micro-crystals lying parallel to the surface. The individual gypsum crystals are acicular. Their size is about 0.4 µm in width and 5 µm in length. They appear entangled yet they leave a significant internal porosity with pore size comparable to that of the micro-crystals.

Figure 2 shows SEM observations of the studied material. As can be seen in Figure 2(a), the material shows a broad range of bubble size, yet most are relatively large (i.e. few hundredths of micrometers), round shaped, well-spaced and rarely interconnected. Figure 2(b) shows that, in addition to the bubbles that have smooth boundaries, smaller pores formed during the setting. A late

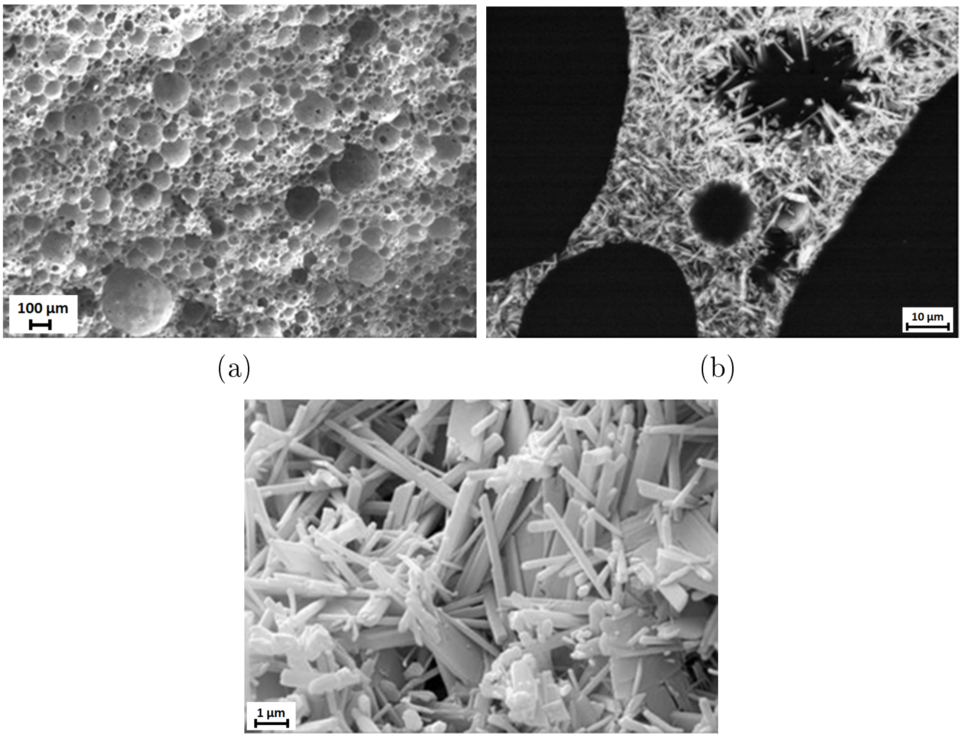

(a) (b)

(c)

Fig. 2. SEM pictures of foamed gypsum at different magnifications

dissolution and crystallization give rise to a very spiky boundary. At an even smaller scale (Figure 2(c)), gypsum crystals are seen to be distributed homogeneously, without preferential direction, presenting typical entanglements that are known to improve the cohesion and resistance of plaster [14].

2.2 In-situ nail pull test

Understanding the failure mechanisms in nail pull tests requires observations in the bulk of the material to be performed since no direct information is available on the external surfaces of samples. This is possible by resorting to X-ray computed tomography [16,17,9]. This technique is particularly appealing in the present case since the material is very heterogeneous (Figure 1). Further, these analyses can even be more informative when *in-situ* mechanical tests are performed during which 3D X-ray tomography scans are acquired at different stages of loading [23].

In the present study, a new setup has been designed to perform *in-situ* nail pull tests within a laboratory X-ray tomograph. The experiment has been conducted on a Phoenix V Tome X® tomograph, using a source setting of 90 KV, 220 µA and a 1920 × 1536 pixel flat panel detector (see Ref. [23] for more details). The physical size of one voxel is 25 µm, which is a good compromise between the thickness of the tested sample (i.e. 13 mm) and the microstructural features of the material (Figure 1). One thousand radiographs are acquired over a 360° rotation of the tomographic stage for each acquisition. The total acquisition time is 60 minutes. A filtered back-projection algorithm enables 3D volumes to be reconstructed [11,12].

The sample used in the reported experiment is prepared from industrial plasterboard plates. The specimen is a cylinder 50 mm in diameter and 13 mm in height. A hole 2.5 mm in diameter is subsequently drilled along its central axis (Figure 3(a)). The sample is then put within the nail pull assembly (Figure 3(b)) made of polymethyl methacrylate (PMMA), which is virtually transparent to X-rays. The nail is made of polyether ether ketone (PEEK), which is a semicrystalline thermoplastic with excellent mechanical properties and has also a low X-ray absorption. The sample is supported over an area of 5 mm around the perimeter of the assembly. Note that the specimen diameter is smaller than specified in the standardized test in order to be properly imaged in the tomograph.

The nail pull assembly (Figure 3 (b)) is positioned in a tension/compression machine inside the tomograph (Figure 4). The test is performed using the testing device developed at MATEIS laboratory (INSA de Lyon) [23] and designed

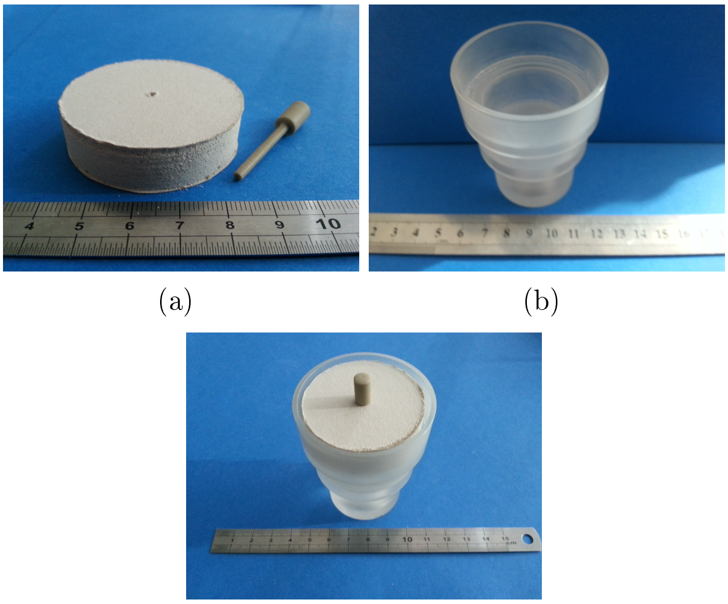

(a) (b)

(c)

Fig. 3. In-situ nail pull setup consisting of a plasterboard circular disk through which a hole has been drilled along the central axis and a PEEK nail (a), a PMMA support (b). Once the disk has been mounted in the PMMA support, the nail head can be pushed through the specimen by an external actuator (c)

to be mounted on the rotary stage of the tomograph. To avoid obstruction of the X-ray beam by the testing machine during the 360° rotation, the compressive load applied onto the nail head is balanced by a tensile load on a cylindrical tube that encloses the test (without contact). This hollow cylinder is made of PMMA so that the X-ray absorption is low as well as uniform, regardless of its angular position. The displacement of the upper platen is provided by a stepping motor controlled by a computer. The latter also records the load.

The nail pull test consisted of pushing the head of the nail into the sample, until failure, with a velocity of 5 µm/s. The load-displacement curve was recorded during the test (Figure 5). In the first part of the test, the sample was imaged at the initial state (i.e. without load) and then at 25 N of loading. Increments of approximately 50 N were applied until the load reached the plateau value

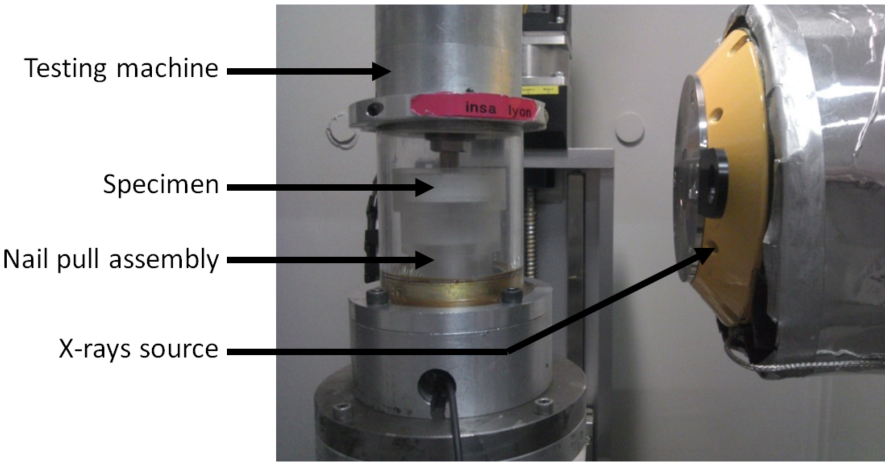

Fig. 4. In-situ nail pull test

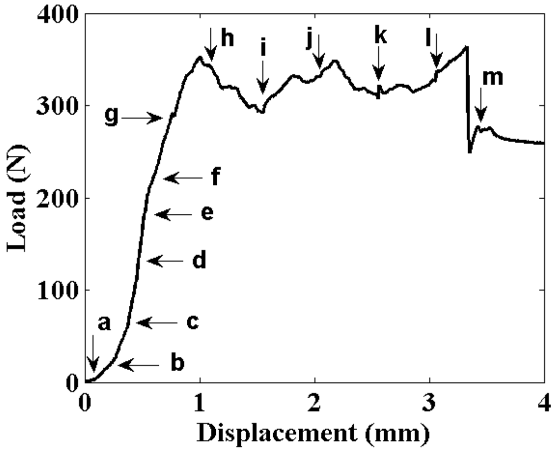

Fig. 5. Load-displacement curve of the test with 13 scans

($\approx$ 350 N in the present case, see Figure 5). Then 0.5 mm displacement increments were applied. After each step, the crosshead was stopped and scans were acquired after a dwell time (about 20 minutes) to prevent blur caused by the relaxation of the sample and the setup during the scan time. The sample was imaged in its initial state (i.e. without load) and at different steps of the experiment. In total, thirteen scans were acquired.

3 Analysis of the failure mechanism

3.1 In-situ observations

Figure 6 shows the microstructural evolution in the same vertical section close to the middle axis of the reconstructed volumes for the different states (from a to m) referenced in Figure 5. The section, which is parallel to the loading axis, has been selected to be located slightly away from the nail axis. All scans, including a, show a small cone crack close to the rear surface presumably due to imperfect hole drilling. It will be shown later that this modest imperfection has no observable influence on the test.

The beginning of the loading curve shows a nonlinear increase corresponding to taking up play between the different moving parts. No microstructural changes are observed in the corresponding scans (see Figure 6, scans a, b, c and d). In particular, no cracks are visually detected in the tomographic pictures.

The second part of the load-displacement curve corresponds to a significant slope change. By analyzing scans e, f and g (Figure 6), and more importantly, by zooming around the nail head (Figure 7), plaster compaction is observed in the upper part of the core. Compaction is caused by pore collapse. Because plaster is compacted, the paper is loaded in tension and breaks. This phenomenon cannot be observed at the chosen resolution, but is deduced from the load drop in Figure 5 (between acquisitions f and g). The roller coating breaks later on close to the nail edges between steps h and i (see Figure 6). The compaction is thus the key point in the failure mechanism of the plate, because it initiates the tearing of the front face paper lining.

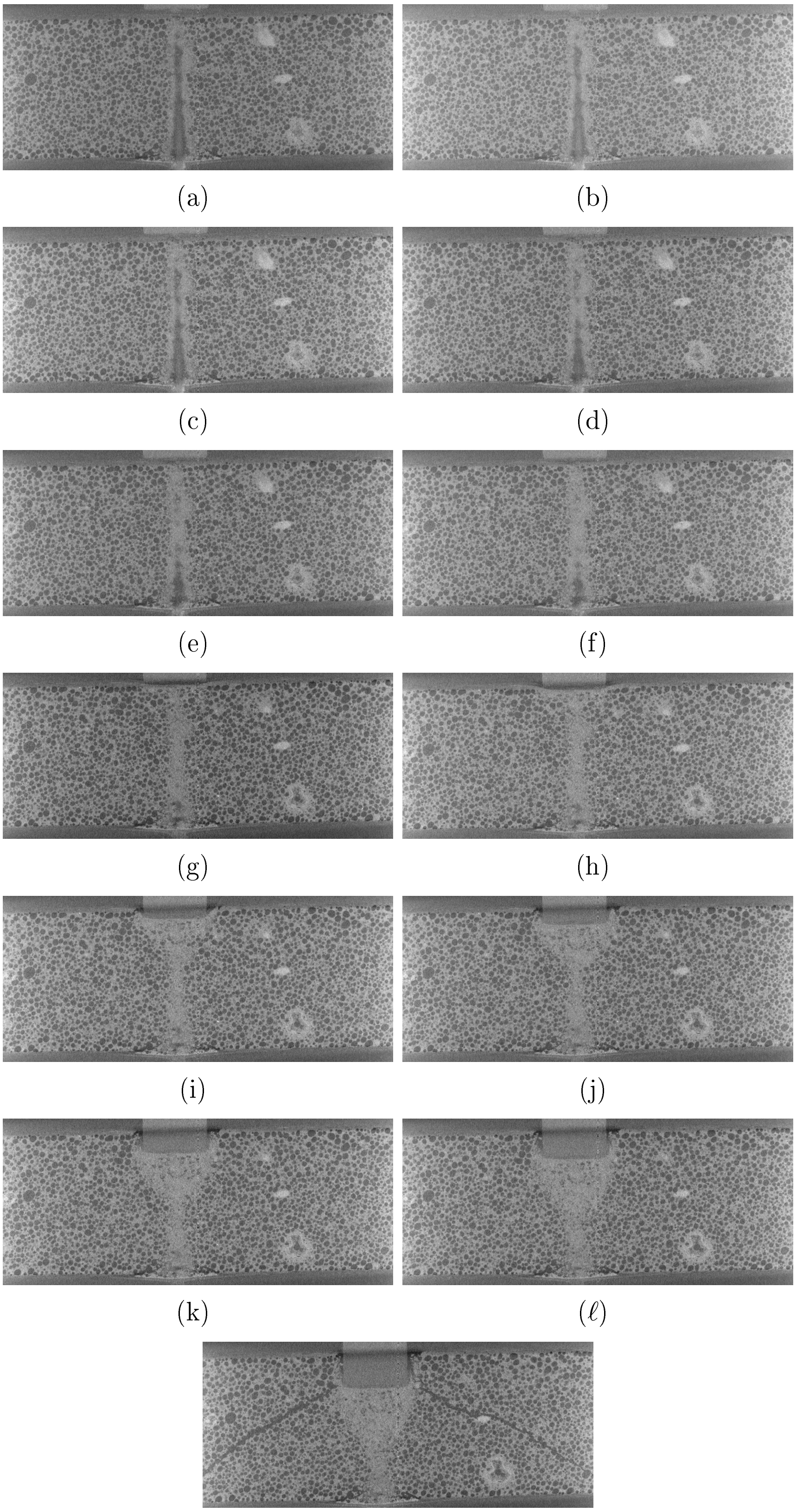

(a) (b) (c) (d) (e) (f) (g) (h) (i) (j) (k) (ℓ) (m)

Fig. 6. Sagittal tomographic sections showing the evolution of the microstructure at different loading levels in the nail pull test. Slice (a) shows the initial state (unloaded state)

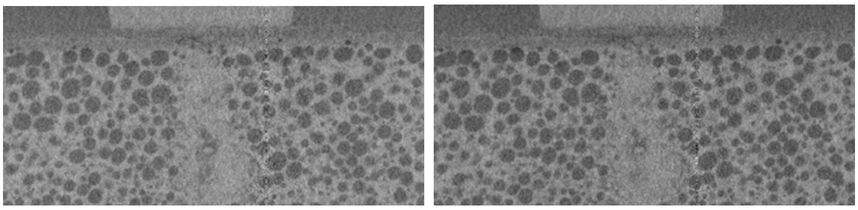

(a) scan (d) (b) scan (e)

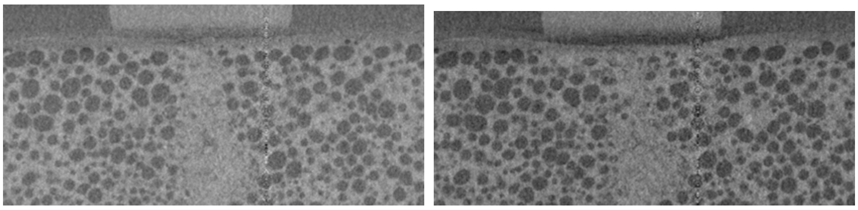

(c) scan (f) (d) scan (g)

Fig. 7. Sagittal tomographic sections showing the evolution of the microstructure under the nail head for scans d to g

As the compaction strength is reached, the upper paper lining (together with the roller-coating) is punched by the nail head, without giving rise to a significant load decrease as the paper is torn down. The applied load is then fully supported by both the core plate and the rear lining. The nail head penetrates through the core of the board sample in a compaction regime that develops over a larger region (see Figure 6, scans h, i, j, k and l). In this regime, the load stabilizes around a level of 350 N with fluctuations. This constant force can be rationalized by noting that the diameter of the compacted region is close to that of the nail head and does not vary in the plateau regime h-l. Simultaneously, the collapsed region gets longer along the nail axis. In other words, the collapsed plaster region propagates along the nail shank toward the bottom face. Thus, the penetration force is expected to remain equal to the crushing strength multiplied by the projected-compaction area in the plane perpendicular to the loading direction. This area is a ring of outer diameter larger than that of the nail head and inner diameter equal to that of the initially drilled hole). The mean compressive strength can be evaluated from the analyses of scan l, for which the outer diameter of the crushed zone is

$\approx$ 8.4 mm (Figure 6(l)). Since the applied load is equal to 320 N, the crushing strength is equal to 6.3 MPa. This value is comparable to crushing strength that was obtained in a spherical indentation test conducted on the same plasterboard [13].

When the nail head has penetrated about one fourth of the sample thickness and the collapsed zone has reached about one half of the sample thickness, the remaining thickness of the plate can no longer withstand the applied load. The final failure is caused by cone-shaped cracking of the core (i.e. opening mode) coaxial with the nail axis (Figure 6, scan m) giving way to the nail through the specimen.

To analyze these observations more deeply, displacement fields and correlation residuals are computed by resorting to digital volume correlation.

3.2 DVC analyses

In the present case, continuous displacement fields are measured when discretized over a finite element mesh made of 8-noded (C8) cubes (i.e. C8-DVC [31]). Since very small strains occur, a regularized approach is preferred [35,36]. The regularization length will be larger than the element size so that the high frequency displacement fluctuations that are not mechanically admissible are filtered out. In the present case, a regularization length of $\ell_{reg} = 30$ voxels was used.

The underlying hypothesis in DVC, namely the conservation of the gray levels of the analyzed microstructure, is exploited by minimizing the correlation residuals (i.e. the sum of squared gray level differences between the reference volume and the deformed volume corrected by the measured displacement field). In the present case, the displacement field is assumed to be continuous thanks to the finite element shape functions of the C8 discretization. Consequently, any discontinuity will be detected in the correlation residuals since the chosen kinematics is not consistent with such a phenomenon [34,37].

To evaluate the measurement resolution, instead of acquiring only one scan in the reference configuration, two scans are acquired without any sample displacement [38]. The DVC code is run on these two scans and any deviation from zero is interpreted as representative of the measurement uncertainty associated with the present setup, data acquisition and processing. The standard displacement resolution is of the order of 0.01 voxel for C8 elements of size equal to 10 voxel and a regularization length of 30 voxels. Correspondingly, the strain measurement uncertainty, as illustrated in Figure 8(a) for the reference volume, is computed to be of order 10^{-3}. Because of the fact that plaster is brittle, and breaks down for low strains, the elastic deformation will not be resolved in the following. Figure 8(b-d) shows that the strain field outside of the compacted zone cannot be measured as being significantly different from 0. Nevertheless, DVC is useful to show, for instance, that cracks with small opening displacement, which would not be visible directly on the tomographic reconstruction, are not present. This uncertainty level is typical of displacement resolutions associated with reconstructed volumes from computed tomography [38]. The root mean square level of the correlation residuals is equal to 9.6 gray levels or 3 % of the overall gray level range.

The displacement field of the n-th scan is assessed by correlating the n-th reconstructed volume with the initial one (unloaded state, scan a, considered as the reference). The Region Of Interest (ROI) over which the displacement

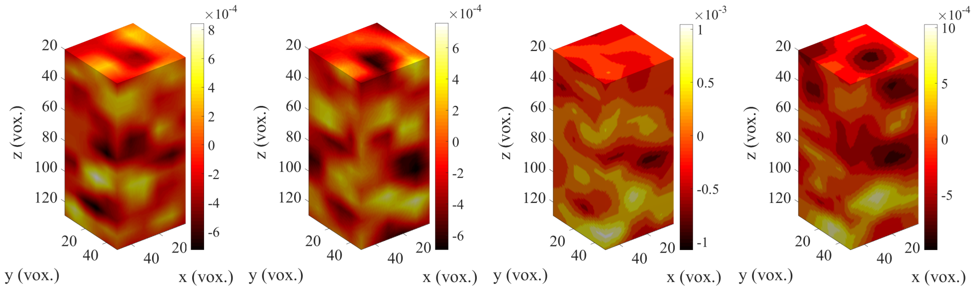

(a) scan a (b) scan d (c) scan g (d) scan j

Fig. 8. (a) 3D renderings of the ϵ_{zz} strain component in the reference configuration measured by RC8-DVC, in order to assess the strain measurement uncertainty. For comparison, a similar plot for the same analyzed ROI located outside of the compacted zone is shown for different stages of loading ((b)-(d)) showing that the strain variation cannot be distinguished from noise. The subvolume analyzed here is located outside the compacted region (in the first quadrant of the global volume)

field is evaluated has a size of $220 \times 220 \times 160$ voxels or $5.5 \times 5.5 \times 4$ mm^3. The size of the C8 cube element is equal to 10 voxels (or 250 µm), the regularization length is equal to 30 voxels (or 750 µm). This choice leads to a little more than 23,000 unknown kinematic degrees of freedom to be measured per analyzed case. Figure 9 shows a 3D renderings of correlation residuals and displacement fields evaluated with RC8-DVC for four steps of the experiment.

Figure 9(a), i.e. state d, shows the displacement fields measured just before the change in slope of the loading curve (Figure 5). The displacement amplitudes are very small (i.e. less than 1 voxel or 25 µm) and are mostly due to a rigid rotation of the sample. Most of the displacement fluctuations are caused by measurement uncertainties, as will be shown below later. Further, the correlation residuals have very small levels (RMS level equal to 9.8 gray levels, which is very close to that observed when no motion was applied to the sample, namely, 9.6 gray levels). In addition, no cracks are detected. From these observations, and those as shown below, it is concluded that up to step d of the nail pull test, the DVC resolution does not allow the motion of the plasterboard core to be distinguished from that of a rigid body.

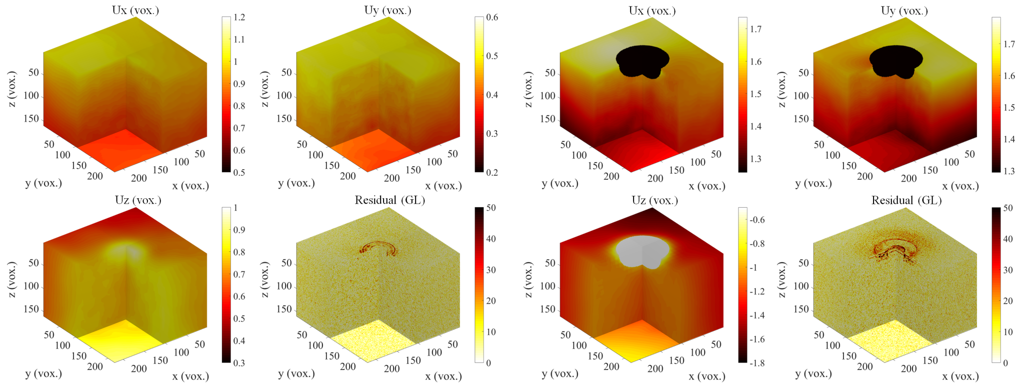

(a) scan d (b) scan g

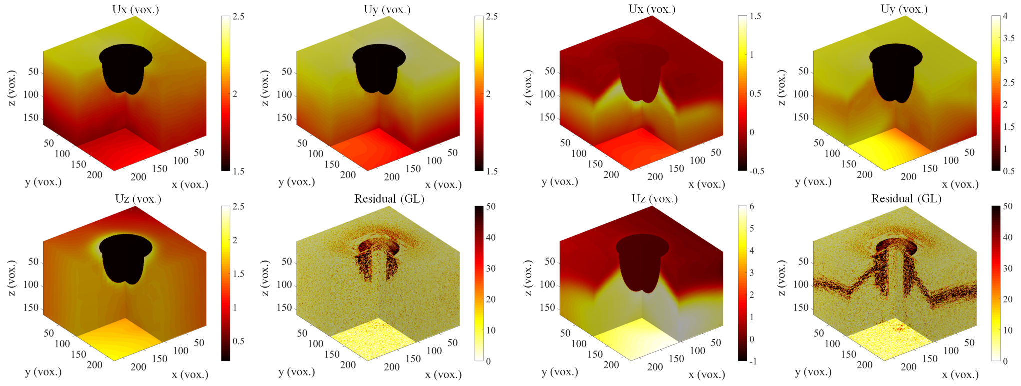

(c) scan j (d) scan m

Fig. 9. 3D renderings of correlation residuals and displacement fields evaluated with RC8-DVC for four steps of the experiment. The loading direction is z and the displacements are expressed in voxels (1 voxel ↔ 25 µm). The correlation residuals are expressed in gray levels (the dynamic range of the reconstructed volumes is 256 gray levels). The compacted zone is masked in the displacements fields

Figure 9(b) (state g) corresponds to the load level just before the tearing of the upper paper lining and roller coating (Figure 6 scan g). Away from the nail head, the measured displacement ranges still have very low levels (i.e. less than one voxel or 25 µm). In the vicinity of the nail head, the correlation residuals increase significantly. In the present case, this result indicates a deviation from the conservation of gray levels due to pore collapse. In this region the initial microstructure is completely lost. Even though a displacement field is reported for this region, it is not trustworthy. In fact, this region is masked for DVC and a basic interpolation is provided to define the displacement over the whole region. This procedure allows for the computation of residuals and thus gives access to the boundary of the crushed region very accurately. A similar procedure was used to analyze the kinematics of an indentation test on the same material [39].

Figure 9 (c) shows the displacement fields measured in the middle of the compaction plateau (Figure 6, scan j). The size of compacted region has significantly increased (as can be judged from the correlation residuals). Its boundary was still sharp with respect to the remainder of the sample, which underwent very small displacement levels. At this late stage of loading, no crack is detected on the correlation residuals (even when this field is carefully inspected in 3D). It is therefore concluded that, at the resolution of the images, no cracking occurred and that the main degradation mechanism was the compaction of the plaster core under the nail head.

The displacement field measured from the last scan, m, has a totally different character as compared to the previous cases (Figure 9(d)). A steep displacement gradient indicative of a discontinuity is clearly observed, which shows the presence of the cone crack leading to the final failure of the sample. The trace of the crack is also present in the correlation residuals. In addition, the compacted zone displays only a slight progression when compared to the previous state l (not shown here). The occurrence of the cone crack can be connected to the very abrupt drop in the penetration force applied onto the nail, as the cone opening gives way to the nail perforation. This observation is consistent with 3D renderings of the corresponding scan in the reference configuration (for which no crack is visible) and the deformed configuration (Figure 10)

Associated with the C8 discretization, the mean Green Lagrange strains are computed over each element [32]. The major positive eigen strain, hereafter termed “equivalent” strain, ϵ_{eq}, is a scalar invariant component that is very

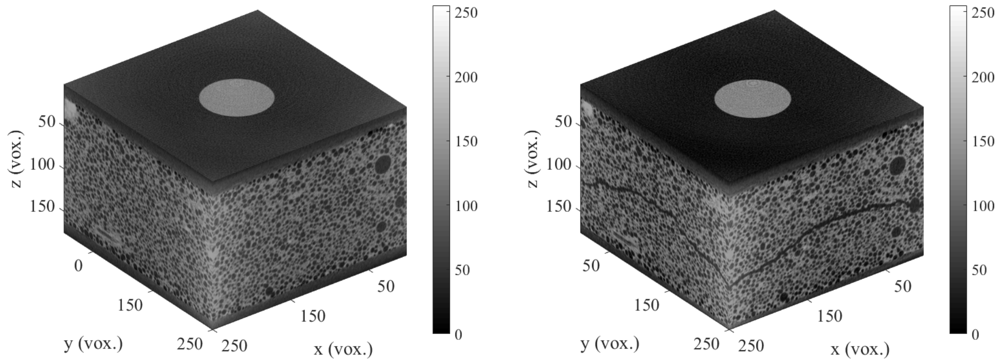

(a) Reference configuration (b) Deformed configuration

Fig. 10. (a) 3D rendering of the microstructure of foamed gypsum to be subjected to nail pull test. (b) The crack is visible on the lateral faces of the sample (the dynamic range of the reconstructed volumes is 256 gray levels)

suited to reveal crack formation irrespective of their orientation. 3D rendering of the equivalent strain is shown in Figure 11. As previously discussed, the crushed region is masked. Outside of it, the amplitude of the equivalent strain (see Figure 11(a), (b) and (c)) measured by RC8-DVC is very low. Because it is the largest (positive) eigenstrain, random fluctuations of zero mean will give rise to a positive mean value for ϵ_{eq} that should not be confused with the statement that strains (apart from the presence of the final cone crack) are indistinguishable from 0. At the last scan, the crack that leads to the breakdown of the sample can be clearly seen from the apparent strain field (Figure 11(d)). It is “apparent” because the displacement discontinuity is distributed over the element size. The crack opening is more easily read from Figure 9(d), although it is not uniform (ranging from 2 to 4 voxels, or 50 to 200 µm), because of a relative rigid body rotation of the two parts.

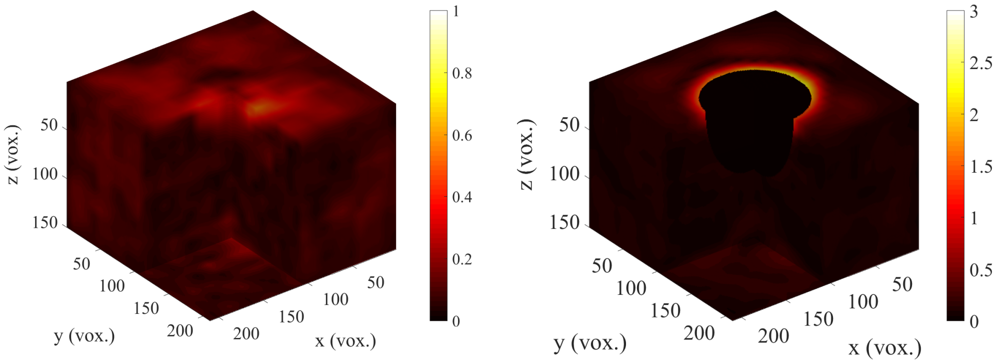

(a) scan *d* (b) scan *g*

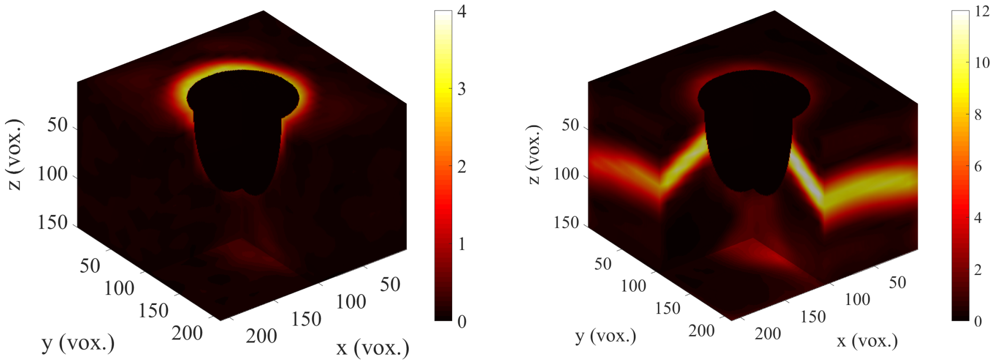

(c) scan *j* (d) scan *m*

Fig. 11. 3D renderings of major principal strain ϵ_{eq} in % obtained from DVC results. Because of the value of the correlation residual is high in the compacted area under the head of the nail, this area is hidden in the major principal strain fields

4 Discussion

Some studies have dealt with the analysis of failure mechanisms in nail pull tests. Peterson [5] carried out many tests (boards with/without top/bottom papers), following the ASTM C473 protocol. The author proposed the following steps based upon the post-mortem analyses. First, the initiation of radial cracks at the rear face of plasterboard was observed for a load level of 130 N. The presence of the rear-side paper prevented complete failure from occurring. Then, at a load varying between 130 N and 230 N, a circumferential crack with a diameter of about 25 mm was visible on the rear face of the plate. With the increase of the load level the crack propagated toward the edge of the nail head. A further increase of the load led to shear failure, which occurred immediately below the nail head when the maximum load was reached ($\approx$ 360 N). In the present case, this chain of events is not observed. For the investigated plasterboard, core cracking occurs at the last loading step. Significant pore collapse is observed prior to the final failure.

Kuntze [3] reported different observations about nail pull tests performed on comparable lightweight plasterboards. The author observed that a cone crack was formed under the nail head, but propagated downward. A similar observation was also reported for gypsum boards by British Plasterboard Research laboratories [6]. In the present analyses it is not possible to conclude whether the final crack has initiated close to the nail head or from the opposite side.

Byford *et al.* [7] also studied the nail pull strength. A series of tests was performed on two types of industrial plasterboard. To investigate the failure mechanism two methods were used, first an SEM analysis was carried out on the polished samples. The second method was X-ray radiography. The latter technique was used for detecting flaws such as cracks and voids. Up to 0.5 mm nail penetration, no irreversible damage or displacement was observed, consistently with a purely elastic behavior. Then, a phase of compaction of the upper part of the core associated with damage and tearing of the upper paper facing was reported. The compaction of the upper part of the gypsum core was considered as the critical factor in the failure mechanism. These observations are identical to the present analyses, in particular the fact that the compaction mechanism is controlling the resistance of plasterboard subjected to nail pull test.

Tests also performed on samples where the lower paper surface was removed showed that shear cracking occurs for similar displacement levels. However, the lower paper facing contributed significantly to the stiffness of the board and hence the result cannot be simply transposed to full plasterboards. Although this study aimed at identifying the failure mechanisms of plasterboard in the nail pull test, the observation of interrupted tests (i.e. for different applied load levels) is difficult and cumbersome (i.e. many samples need to be analyzed), and the onset of the different stages is unprecise. The method used to test the plasterboards was not really applicable to identifying the critical stage of failure as the interruption at very few stages gives a coarse view, and the considered penetrations were too aggressive as compared to the typical encountered failure loads. In the present case, tomography coupled with in-situ nail pull test allows the various mechanisms to be analyzed non destructively on a single sample.

Cantwell [8] conducted a comparable study to that of Reference [7] aiming for the identification of the different stages of failure in nail pull tests on three types of industrial plasterboard. Interrupted tests were selected as the strategy to have access to the different stages of degradation. Microcracking and/or local collapse of the porosity was the first observed step in the failure process. At 40% of the ultimate load, the author observed pore collapse and the formation of a compacted zone in the area of the nail head. Crushing of the plaster foam resulted from inter-crystalline slip, intra-crystalline shear and/or fracture of gypsum crystals. The author interpreted the following stage as the collapse of the porous plaster, together with the coalescence of microcracks. At 80% of the ultimate load the top paper was finally perforated along the edge of the nail head. A densified region developed under the nail head, which was completely separated from the upper paper. At the end of the test permanent strains were observed in the paper and the core of the plate. Lateral cracks appeared in the top roller coating layer and at the interface between the roller coating and the core of the plate. High densification due to the collapse of the porosity under the nail head was also reported. In the present case, the same degradation scenario is observed. However, given the chosen resolution (i.e. 25 µm) it is not possible to discuss the microscopic origin of the mesoscopic obervations. High resolution tomography may allow for such investigations.

5 Conclusions and perspectives

In this work a comprehensive analysis of the standardized nail pull test has been proposed. Thanks to X-ray tomography, *in-situ* mechanical testing and digital volume correlation, the degradation mechanisms of lightweight plasterboard in the nail pull test have been identified. After contact between the nail head and the sample surface, no evidence of damage is observed up to about half of the peak load. As soon as compaction of the core starts, as observed through the inception of a densified layer under the nail head, the top paper lining is torn and the roller coating fails. This compaction is thus very clearly the critical factor that controls the plateau stress, with no sign of load overshoot when the paper facing and roller coating give way to the nail. After this stage, the penetration of the nail takes place under constant load, which corresponds to the compaction phase of the plaster core in a cylindrical region of fixed diameter close to that of the nail head, and increasing length as the nail penetrates further in the core. When the penetration reaches a depth of about 25 % of the initial thickness of the plasterboard, the final failure of the sample, by cone cracking of the core, occurs abruptly. The post-crack resistance only comes from the paper backing, which has to be torn down to free the nail.

The above conclusions are drawn from the analysis of reconstructed volumes acquired at different steps of the nail pull test. The analysis of tomographic observations by digital volume correlation was also conducted and shows, in particular, that local crushing of the upper part of the core of the plate is located directly under the nail head prior to the failure of the front paper lining. Measured displacement fields confirm the degradation mechanisms observed from the tomographic scans. They also indicate that no crack initiates until the very end of the experiment at the chosen resolution (i.e. 25 µm per voxel) Consequently, the compaction role of the plaster foam core entirely determines the nail pull resistance for the system under study.

The fact that compaction is observed in the nail pull test reported herein and in an indentation test on the same material [39] proves that the latter is representative of the former, even though the indenter shape is very different. This can be explained by the fact that as soon as the compaction zone develops, the role of the indenter itself is minimal since the boundary of compacted zone is itself the effective indentor further loading the intact foamed plaster. The fact that a compaction zone grows is beneficial to the plasterboard as it does not localize in very small regions where the material may no longer be able to sustain the applied load. The observed plateau of the penetration force for a displacement covering a significant fraction of the board thickness prevents a brittle failure that would be detrimental to safety.

Whilst the observations and conclusions made herein are specific to the studied plasterboard, the present methodology, where a wealth of information is accessible, may be followed to analyze other brittle foams. For such problems where different mechanisms are intricate, the geometry is confined and hidden to surface observations, mechanical tests conducted in-situ in a tomograph are invaluable.

Acknowledgements

The authors wish to thank Saint-Gobain Recherche for supporting this research project, and particularly René Gy for insightful discussions. AB is also financially supported by ANRT through contract no. 2010/567. The authors would also like to thank Dr. S. Meille for helpful discussions.

References

[1] ASTM Standard C473-10, Standard Test Methods for Physical Testing of Gypsum Panel Products ASTM International, West Conshohocken, PA, 2010, DOI: 10.1520/C0473-10, www.astm.org

[2] Wenk, R.J. Gypsum board – Opportunities and Challenges. *XIII Eurogypsum Congress*, 1987.

[3] Kuntze, R.A. Gypsum: Connecting Science and Technology *ASTM International 100 Barr Harbor Drive PO Box C700 West Conshohocken, PA*, 2009.

[4] ASTM Standard C1396/C1396M-14, Standard Specification for Gypsum Board, ASTM International, West Conshohocken, PA, 2014, DOI: 10.1520/C1396_C1396M, www.astm.org

[5] Peterson, K. Enginneered Gypsum Panels. *Sixth International Conference on Gypsum, Ortech, International, Toronto, May 2000.*

[6] Private communication from BPB Research Centre, London.

[7] Byford et al. Private communication from BPB Research Centre, London.

[8] Cantwell, P. Failure Mechanism of Nail Pull. *BPB Group Technical Department, Report number: 21717*, 2003.

[9] Maire, E., Withers, P. J. Quantitative X-ray tomography. *International Materials Reviews*, 59(1), 1-43, 2014.

[10] Buffière, J.Y. and Maire, E. and Adrien, J. and Masse, J.P. and Boller, E.. In Situ Experiments with X ray Tomography: an Attractive Tool for Experimental Mechanics. *Exp. Mech.*, 50(3), 289-305, 2010.

[11] Feldkamp, L.A. and Davis, L.C. and Kress, J.W. Practical cone beam algorithm. *J. Opt. Soc. Am.*, A1, 612-619, 1984.

[12] Kak, A.C. and Slaney, M. Principles of computerized tomographic imaging. *IEEE Press*, New York, 1988.

[13] Bouterf, A. and Adrien, J. and Maire, E. and Brajer, X. and Hild, F. and Roux, S. Identification of the crushing behavior of brittle foam. From indentation to oedometric tests. *Submitted*, 2016.

[14] Meille, S., Garboczi, E.J. Linear elastic properties of 2D and 3D models of porous materials made from elongated objects. *Modeling and Simulation in Materials Science and Engineering*, 9, 371-90, 2001.

[15] Desrues J. Tracking Strain Localization in Geomaterials Using Computerized Tomography. In: *X-ray CT for Geomaterials*, Otani, J. and Obara, Yuzo Ed., Balkema, 15-41, 2004.

[16] Desrues, J. and Viggiani, G. and Bésuelle, P. Advances in X-ray Tomography for Geomaterials. *Wiley / ISTE*, London (UK), 2006.

[17] Stock, S.R. Recent advances in X-Ray microtomography applied to materials. *Int. Mat. Rev.*, 53(3), 129-181, 2008.

[18] Colliat-Dangus, J.L., Desrues, J., Foray, P. Triaxial Testing of Granular Soil Under Elevated Cell Pressure. *Advanced Triaxial Testing of Soil and Rock ASTM STP 977*, Robert T. Donaghe, Ronald C. Chaney, and Marshall L. Silver, Eds, American Society for Testing and Materials, Philadelphia, 290-310, 1988.

[19] Desrues J., Chambon R., Mokni M., Mazerolle F. Void ratio evolution inside shear bands in triaxial sand specimens studied by computed tomography. *Géotechnique*, 46(3), 529-546, 1996.

[20] Guvenilir, A., Breunig, T. M., Kinney J. H., Stock S. R. Direct observation of crack opening as a function of applied load in the interior of a notched tensile sample of Al-Li2090. *Acta Materialia*, 45, 1977-1987, 1997.

[21] Bay, B. K., Smith, T. S., Fyhrie D. P., Saad, M. Digital Volume Correlation: Three-dimensional Strain Mapping Using X-ray Tomography. *Experimental Mechanics*, 39, 217-226, 1999.

[22] Elliot, J.A., Windele, A.H., Hobdell, J. R., Eeckhaut, G., Olman, R. J., Ludwig, W., Boller, E., Cloetens, P., Baruchel, J. In-situ deformation of an open-cell flexible polyurethane foam characterized by 3D computed microtomography. *Journal of Material Science*, 37, 1547-1555, 2002.

[23] Buffière, J. Y., Maire, E., Adrien, J., Masse, J. P, Boller, E. In Situ Experiments with X ray Tomography: An Attractive Tool for Experimental Mechanics. *Experimental Mechanics*, 50, 289-305, 2010.

[24] Smith, T. S., Bay, B. K., Rashid, M. Digital volume correlation including rotational degrees of freedom during minimization. *Experimental Mechanics*, 42, 272-278, 2002.

[25] Sutton M.A., Orteu J.J., Schreier, H. Image correlation for shape, motion and deformation measurements: Basic Concepts, Theory and Applications. *Springer*, 2009.

[26] Bornert, M., Chaix, J. M., Doumalin, P., Dupré, J. C., Fournel, T., Jeulin, D., Maire, E., Moreaud, M., Moulinec, H. Mesure tridimentionnelle de champs cinématiques par imagerie volumique pour l'analyse des matériaux et des structures. *Inst. Mes. Métrol*, 4, 43-88, 2004.

[27] Verhulp, E., van Rietbergen, B., Huiskes, R. A three-dimensional digital image correlation technique for strain measurements in microstructures. *J. Biomech.*, 37(9), 1313-1320, 2004.

[28] Franck, C. and Hong, S. and Maskarinec, S.A. and Tirrell, D.A. and Ravichandran, G. Three-dimensional Full-field Measurements of Large Deformations in Soft Materials Using Confocal Microscopy and Digital Volume Correlation. *Exp. Mech.*, 47, 427-438, 2007.

[29] Germaneau, A. and Doumalin, P. and Dupré, J.C. Full 3D measurement of strain field by scattered light for analysis of structures. *Exp. Mech.*, 47(4), 523-532, 2007.

[30] Hall, S. and Bornert, M. and Desrues, J. and Pannier, Y. and Lenoir, N. and Viggiani, C. and Bésuelle, P., Discrete and continuum analysis of localised deformation in sand using X-ray micro CT and volumetric digital image correlation. *Géotechnique*, 60(5), 315-322, 2010.

[31] Roux, S., Hild, F., Viot, P., Bernard, D. Three-dimensional image correlation from X-ray computed tomography of solid foam. *Composites Part A* 39, 1253-1265, 2008.

[32] Hild, F., Maire, E., Roux, S., Witz, J. F. Three dimensional analysis of a compression test on stone wool. *Acta Materialia*, 7, 3310-3320, 2009.

[33] Limodin, N., Réthoré, J., Buffière, J.-Y., Gravouil, A., Hild, F., Roux, S. Crack closure and stress intensity factor measurements in nodular graphite cast iron using 3D correlation of laboratory X ray microtomography images. *Acta Materialia*, 57, 4090-4101, 2009.

[34] Rannou, J., Limodin, N., Réthoré, J., Gravouil, A., Ludwig, W., Baïetto-Dubourg M.C., Buffière, J.Y., Combescure, A., Hild, F., Roux, S. Three dimensional experimental and numerical multiscale analysis of a fatigue crack.

Computer Methods in Applied Mechanics and Engineering, 199, 21-22, 1307-1325, 2010.

[35] Leclerc, H., Périé, J.N., Hild, F., Roux, S. Digital Volume Correlation: What are the limits to the spatial resolution? *Mech. & Indust.*, 13, 361-371, 2012.

[36] Taillandier-Thomas, T., Roux, S., Morgeneyer, T.F., Hild, F. Localised strain field measurement on laminography data with mechanical regularization. *Nuclear Instruments and Methods in Physics Research Section B*, 324, 70-79, 2014.

[37] Hild, F., Fanget, A., Adrien, J., Maire, E., Roux, S. Three dimensional analysis of a tensile test on a propellant with digital volume correlation. *Archives of Mechanics*, 63(5-6), 1-20, 2011.

[38] Limodin, N., Réthoré, J., Adrien, J., Buffière, J.Y., Hild, F., Roux, S. Analysis and artifact correction for volume correlation measurements using tomographic images from a laboratory X-ray source. *Experimental Mechanics*, 51(6), 959-970, 2011.

[39] Bouterf, A., Roux, S., Hild, F., Adrien, J., Maire, E., Meille, S. Digital Volume Correlation Applied to X-ray Tomography Images from Spherical Indentation Tests on Lightweight Gypsum. *Strain*, 50(5), 444-453, 2014.